International Journal of Fatigue 142 (2021) 105949

Contents lists available at ScienceDirect

International Journal of Fatigue

journal homepage: www.elsevier.com/locate/ijfatigue

The effect of forging texture and machining parameters on the fatigue performance of titanium alloy disc components

Daniel Suárez Fernández[a,c,*], B.P. Wynne[a,b], P. Crawforth[c], K. Fox[d], M. Jackson[a]

[a] Department of Materials Science and Engineering, The University of Sheffield, Sir Robert Hadfield Building, Mappin St, Sheffield S1 3JD, UK
[b] Department of Mechanical and Aerospace Engineering, University of Strathclyde, Glasgow G1 1XJ, UK
[c] Advanced Manufacturing Research Centre, Advanced Manufacturing Park, Catcliffe, Rotherham S60 5TZ, UK
[d] Rolls-Royce plc, PO Box 31, Derby DE24 8BJ, UK

ARTICLE INFO

Keywords:
Titanium alloys
Forging
Machining
Low cycle fatigue

ABSTRACT

The Mechanisms of fatigue failure in Ti-6Al-2Sn-4Zr-6Mo forged discs are investigated: the effects of forging and machining operations on fatigue are decoupled. A four-point bend fatigue testing approach enabled the crack initiation and propagation characteristics to be studied at multiple locations around the disc periphery. Fatigue performance variation (of ~60%) at different positions, and crack initiation and propagation behaviour were linked to the heterogeneous crystallographic texture - developed during upstream forging. Downstream machining processes were found to increase fatigue life, regardless of the cutting speed. However, circumferential fatigue heterogeneity, inherent from the forging stage was still evident even after machining.

1. Introduction

Titanium alloys are used in high performance rotating components in the aerospace industry, particularly compressor discs, as they possess high strength/weight ratios and excellent fatigue and corrosion resistance. Such components are highly regulated through organisations like the European Aviation Safety Agency and the Federal Aviation Administration, and in terms of economics, are a significant fraction of the cost of aircraft production and operation. Their in-service failure is highly unlikely but the consequences when a failure occurs are catastrophic; and therefore, such parts are classified as safety–critical [1], and thus, stringent manufacturing standards and rigorous none destructive evaluation (NDE) methods are applied. As an example, the initial vacuum arc remelted (VAR) ingot's microstructure must show levels of the order of less than one defect per 500 t of melted weight [2,3].

Primary forging starts with a cogging operation of the VAR ingot using an open die hammer press at forging temperatures above the β transus, where the ingot is rotated and moved forward between two (or four) open dies, schematically represented in Fig. 1a. The cogging process homogenises the as-cast chemistry and breaks-up the heterogeneous columnar microstructure of the ingot into a refined equiaxed β grain structure [4]. Depending on final microstructure requirements, temperatures will be maintained above the β transus to obtain a final room temperature microstructure of lath-like α. Following the initial forging steps, the final forging stages are undertaken at subtransus temperatures to produce a microstructure of equiaxed primary α in a matrix of secondary α (or transformed β). The initial VAR ingot cross section is cogged down from approximately 1000 mm diameter through a complex shaping operation to approximately 250–300 mm diameter cylindrical billet. The complex nature of the forging means there can be significant variations in total strain experienced along the radial direction from the centre to the surface and non-linear strain-path circumferentially, leading to variations in β grain size and β crystallographic texture throughout the billet.

During secondary forging stages, a length of the cogged billet is extensively processed through a combination of upsetting and hot closed die forging operations to achieve a shape as close to the final component as possible. The workpiece temperature can be either super- or subtransus depending on the complexity of the final shape and desired final microstructure and property requirements. Closed die forging can also induce significant variation in strain, strain rate, and temperature throughout the section, further exacerbating the heterogeneous strain patterns within the final forging.

On cooling to room temperature, a variation in α texture is also developed in the near net shape component. This is because the phase transformation from BCC β to HCP α follows the strict Burgers orientation relationship where $(1\ 1\ 0)_\beta||(0\ 0\ 0\ 2)_\alpha$ and $\langle 1\ 1\ 1\rangle_\beta||\langle 1\ 1\ \bar{2}\ \bar{0}\rangle_\alpha$, meaning only 12 α orientation variants are possible from the parent β grain. A strong β texture can therefore only

* Corresponding author.
E-mail address: D.Suarez@sheffield.ac.uk (D. Suárez Fernández).

https://doi.org/10.1016/j.ijfatigue.2020.105949
Received 16 May 2020; Received in revised form 8 September 2020; Accepted 10 September 2020
Available online 18 September 2020
0142-1123/ © 2020 The Author(s). Published by Elsevier Ltd. This is an open access article under the CC BY license (http://creativecommons.org/licenses/BY/4.0/).

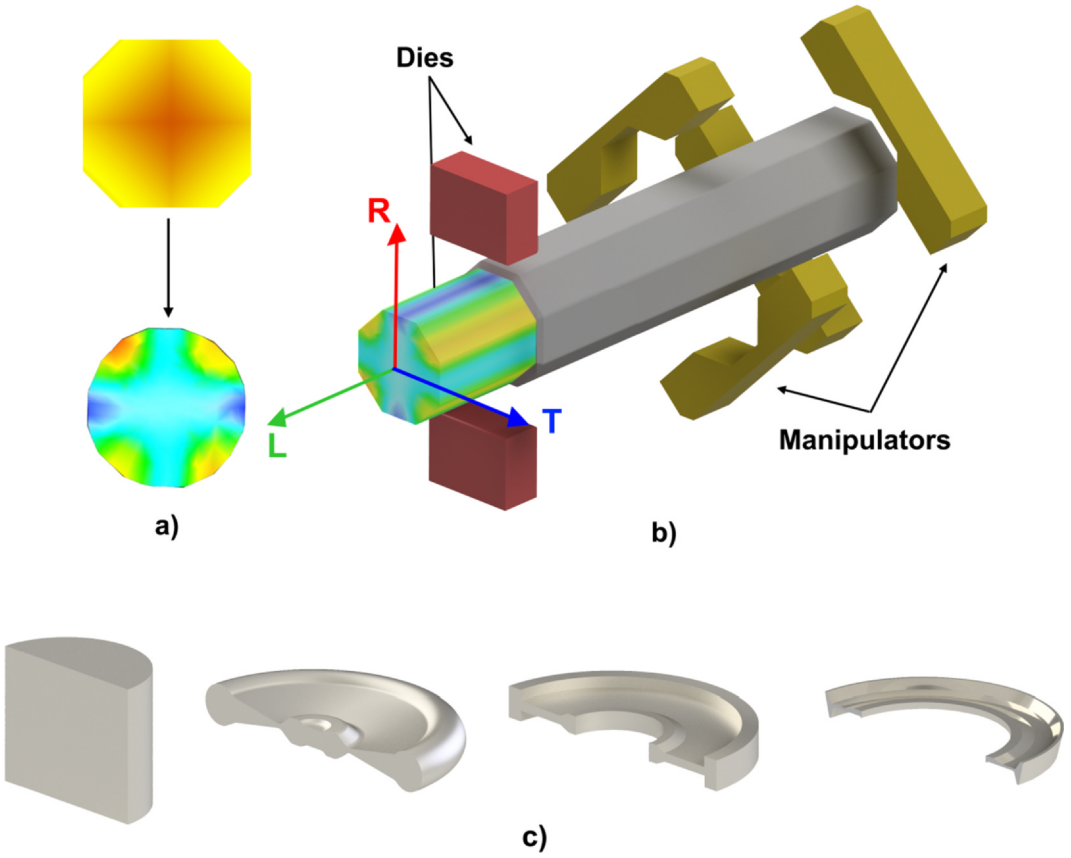

Fig. 1. (a) Initial VAR ingot square cross section with no strain induced top and DEFORM® simulation of the cross-section strain induced during the primary forging performed by TIMET ® (bottom) [orange/yellow colouring relates to total high strain regions]. (b) 3D schematic of a typical open die forge / titanium alloy workpiece interaction during the primary forging process with strain induced overlaid. [18] (c) Schematic of the cross section evolution of the component during its manufacturing steps, from left to right (1) after primary forging, (2) after forging, (3) after roughing to a rectilinear shape, and (4) final machined compressor disc component.

be diluted by a maximum factor of 12. However, not all of the possible directions are developed per parent β grain; this phenomenon is known as variant selection – which could lead to the potential for a relatively strong α texture [5–7]. Furthermore, owing to the multi-step primary and secondary forging stages and the high temperature at which they are maintained, the β grain size at the end of the forging stage is still relatively large, particularly for alloys processed above the β transus. This combined with a relatively slow cooling rate, even during water quenching, promotes the formation of large colonies of similarly orientated α laths within the prior β grain, owing to the low thermal conductivity of titanium. Each colony of α laths acts as an effective structural unit (ESU) with a size that has significant impact on fatigue life, affecting crack initiation and propagation mechanisms [2].

After closed die forging the disc is machined to defined tolerances in order to allow NDE ultrasonic inspection, the component at this stage is often referred to as a "rectilinear forging". The rectilinear forging is further machined in two stages, with approximately 80% of the closed die forging being machined away (Fig. 1b). The initial *rough* machining stage removes a large volume of material at relatively high depths of cut. The final *finish* machining stage defines the final surface conditions of the component and final geometry. Finish machining is generally carried out at much lower depths of cut whilst employing careful control of the cutting speed and feed so as to not induce excessive subsurface microstructural deformation, Fig. 1b.

There have been several studies on the machinability of titanium alloys from a tool life standpoint [8–11]. For, example, Arrazola et al. [12] showed that the rate of tool wear was greater for the high strength metastable β alloy Ti-5Al-5V-5Mo-3Cr (Ti-5553) compared to Ti-6Al-4V, implying that there is a relationship between machinability rate, materials properties and alloy chemistry. Armendia et al. [13] showed significant tool wear in Ti-6246 when machining at speeds higher than 90 m/min and that significant changes in microstructure induced by heat treatment significantly impacted on the tool wear performance. Furthermore, recent studies have broadened the machinability assessment to understand and link the effects of machining parameters on subsurface deformation with respect to the crystallographic texture in the workpiece [14–16].

However, from a process cycle life standpoint, machinability has to take into account the impact of machining parameters on in-service behaviour of the final component. Up to now, the direct response of machining of titanium alloys on fatigue and crack initiation and propagation behaviour has not been widely reported in the literature. Cox et al. [17] correlated metal removal rates with fatigue performance through a 4-point bend fatigue testing approach. It was found that increasing metal removal rate at the finish milling stage, reduced the fatigue life (i.e. cycles to failure) in the high strength metastable β alloy Ti-5553. This was studied by machining the coupons under different conditions to impart different levels of surface and sub-surface deformation to replicate industrial milling parameters in aerospace landing gear forged components. Low cycle fatigue (LCF) properties, crack initiation mechanisms and favourably slip plane microcrack initiation in specific locations of the forging under different machining conditions were characterised. This is important as the impact of machining parameters on the surface condition and subsurface microstructure cannot be easily replicated in conventional dog-bone type fatigue specimens, for example.

In this study, a 4-point bend fatigue testing approach was used on Ti-6Al-2Sn-4Zr-6Mo (Ti-6246) compressor disc forgings to investigate

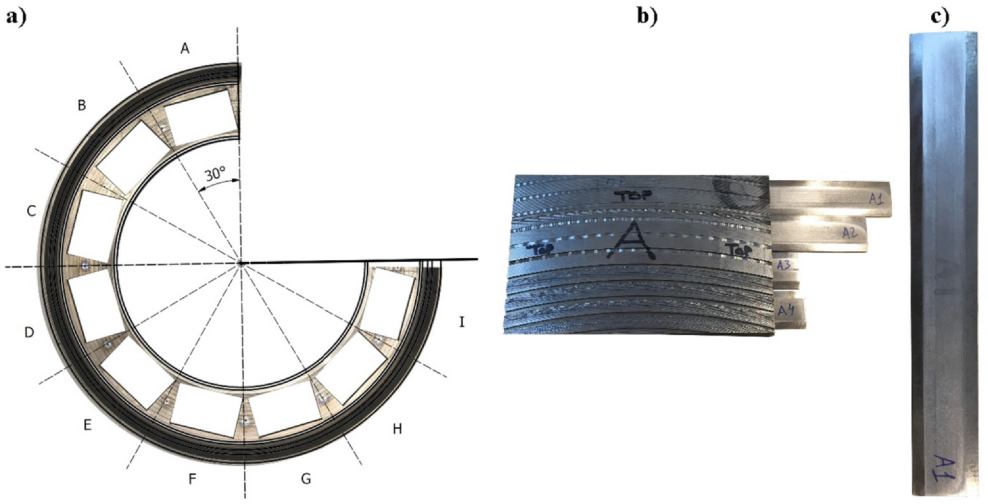

Fig. 2. (a) Photograph of disc 1 after the blocks have been extracted using EDM technique; (b) an example of an extracted EDM'ed block (location A) with the corresponding four coupons and (c) photograph of a 4-point bend coupon.

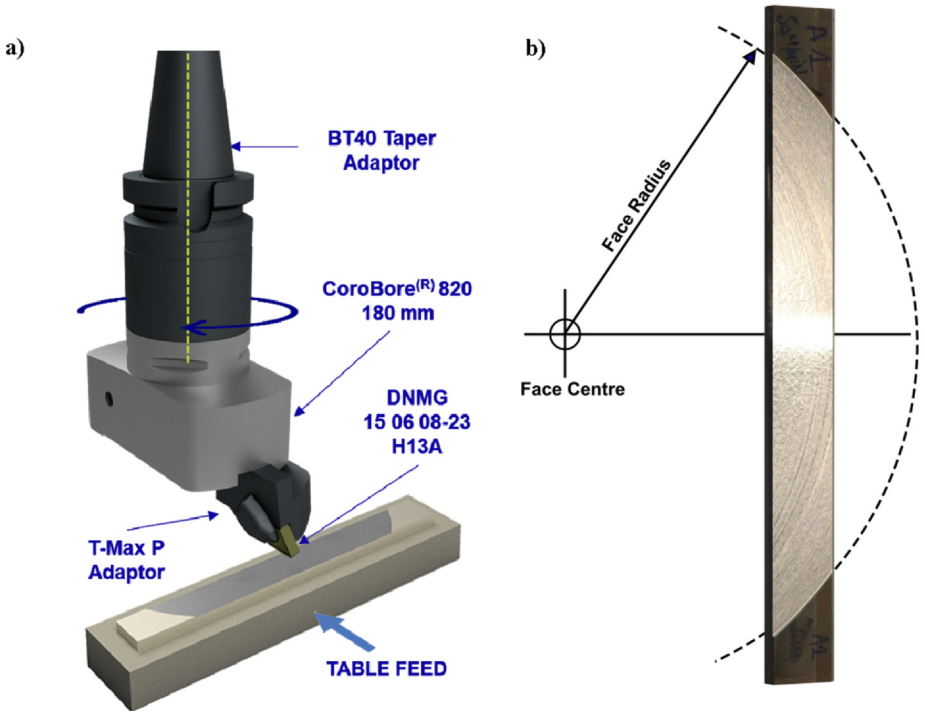

Fig. 3. (a) Schematic of the boring head machining a Ti-6246 coupon with corresponding rotation and coupon advancing direction shown and; (b) photograph of a machined coupon surface prior to trimming to final dimensions and overlaid onto the equivalent face turned radius.

the cumulative effect of crystallographic texture developed during the forging processes and subtractive machining processes on fatigue behaviour and crack propagation mechanisms. The investigation was conducted in collaboration with key companies in the aerospace manufacturing supply chain in order to determine the effects of through processing on service performance.

2. Experimental procedures

2.1. Material as-received and coupon extraction

This study used two semi-finished super β transus forged Ti-6246 rectilinear aero-engine intermediate pressure compressor discs made from Ti-6246, supplied by Rolls-Royce plc. Disc 1, of which only three quarters was available for investigation, was used for the as-forged analysis and the machining trials were undertaken on a complete second disc (disc 2).

For the as-forged analysis of disc 1 a set of four samples were extracted from each of nine radial directions in the middle section diaphragm using Electrical Discharge Machining (EDM) at 30° spacing, as shown in Fig. 2. Sample dimensions were 130 × 19 × 3.6 mm, a light grinding process was applied to remove the re-cast layer generated by the EDM and to provide each coupon with the same surface finish and roughness in order to reduce variability due to surface finish. As the coupons were extracted from the centre of the diaphragm, any machining process will not affect the extracted material; hence it can be considered that the response of these coupons is representative of the "as-forged" bulk material.

A similar approach was followed for disc 2 samples that would then be subsequently machined. Four coupons with dimensions of

Table 1
Machining conditions applied to every set of 4 coupons.

	Cutting speed Vc [m/min]	Depth of cut Ap [mm]	Feed [mm/rev]	Metal Removal Rate [mm^3/min]
COUPON 1	50	0.5	0.15	3750
COUPON 2	70	0.5	0.15	5250
COUPON 3	90	0.5	0.15	6750
COUPON 4	150	0.5	0.15	11,250

180 × 19 × 3.6 mm, were extracted from each of nine different radial directions separated by an angle of 40°. In this case, the extracted length of the coupons was 180 mm, in order to clamp them to a rigid fixture and apply the required machining conditions to the top surface of the coupon, before trimming to the 130 mm length.

2.2. Machining process

The machining operation applied to the top surface of the coupons replicated a standard face turning operation [19] using a CNC MORI DMG NVX 7000 machining centre. The machining set up consisted of a 132 DNMG 15 06 08-23 H13A insert held within a T-Max P® SL-PDJNR-32-15HP tool holder. This was installed in a Sandvik CoroBore® 825 boring head coupled to BT 40/MAS-BT403 taper 134 in order to connect the tool to the main spindle of the machine. A new cutting edge was used to machine each coupon, as depicted in Fig. 3. The machining conditions applied are summarised in Table 1.

To translate the machining dynamics of an equivalent turning process transferred into a standard CNC milling machine using a boring head, it is necessary to link the turning machining variables feed per revolution and cutting speed (f_{rev} [mm/rev] and V_c [m/min]), with milling variables spindle and table feed (RPM and table V_{feed} [mm/min]). Eqs. (1) and (2) show the geometric transformation for equivalent machining parameters.

$$RPM_{milling} = Vc_{Turning} \left[\frac{\text{m}}{\text{min}}\right] \cdot \frac{1}{2 \cdot \pi \cdot radius_{boring\ \ head}\ [\text{m}]} \tag{1}$$

$$V_{feed} \left[\frac{\text{m}}{\text{min}}\right] = f_{rev} \left[\frac{\text{m}}{\text{rev}}\right] \cdot RPM_{milling} \tag{2}$$

By using these calculations, it is possible to impart the same cutting parameters and material removal rates which are comparable to those used in industrial turning operations. Thus, providing an analogous tool material machining interaction on the top surface of the extracted coupons which matches the surface of the extracted coupons obtained from a face turned disc component machined at *Rolls-Royce*.

2.3. Four-point bend test methodology

The 4-point bend test set up uses four 10 mm rollers (BS 8734/ISO 8734), where the top and bottom sets are separated by 80 mm and 40 mm, respectively. Needle roller bearings SKF® BK1012 support the rollers to simulate a contact under zero friction. Table 2 summarises the testing parameters used in this test.

The testing coupons are rectangular with a length of 130 mm, a width of 19 mm and a thickness of 3.6 mm. The top corners of the cross section were chamfered to avoid stress concentration points on the top surface edges. The yield strength for Ti-6246 with a bimodal microstructure is reported in the literature to be approximately 1100 MPa [20]. The exact yield strength of the analysed disc material with a large prior β grain and basketweave microstructure is higher – unfortunately, the actual value cannot be published due to commercial confidentiality. A schematic of the coupon geometry, stress distribution and rollers can be seen in Fig. 4.

Table 2
Dynamic loading conditions selected for the 4-point bend test.

F_{max} [N]	F_{min} [N]	R ratio	σ_{max} [MPa]	σ_{min} [MPa]	Freq. [Hz]	Waveform
4260	426	0.1	1038	103.8	5	Sinusoidal

2.4. Microstructural analysis

Microstructure analysis was performed using cross polarised light microscopy. The alloy was metallographically prepared with colloidal silica and a mixture of 10% of hydrogen peroxide to achieve mirror finish prior to etching using Kroll's Reagent. Secondary electron images of fracture surfaces were carried out in a FEI Inspect F50 scanning electron microscope (SEM). These images were taken with an accelerating voltage of 20 kV and a spot size of 5.0.

This same SEM was also used for performing the texture analysis using an EBSD detector to perform bulk texture analysis and more accurate analysis for crack propagation study. Large EBSD maps were performed across 10 × 8 mm areas using a step size of 17 μm (0.154 s/pt.). The high accuracy analysis of the crack propagation crystallography was mapped a region of 0.5 × 1.1 mm with a step size of 1.2 μm (0.12 s/pt.). A FEI Inspect F50 and same accelerating voltage and spot size was used as before (20 kV and 5.0). Channel 5 software [21] was used for analysing the EBSD data.

The microstructure at different angular locations of the disc is shown in Fig. 5. The analysed discs exhibit a β processed Widmanstätten microstructure with a prior β grain size of an average size of 1174 μm in the radial axis and 540 μm in the longitudinal direction. This means that the average aspect ratio of the prior β grains is 0.46. There are no clear microstructural variations around the disc and the grain size, aspect ratio and secondary α morphology is consistent under cross-polarised light examination – such consistency is expected from a robustly manufactured aerospace critical component. Chemical analysis performed using X-EDS also showed no variability in chemistry composition at different circumferential locations.

3. Results

3.1. Analysis of the mechanical properties in the as-forged condition

Fatigue samples extracted from disc 1 were tested under dynamic conditions provided in Table 2 until failure. The cycles to failure are plotted in Fig. 6b with error bars, in red. The error bars represent the standard error of the measurements per direction.

A total variation of up to 60% in cycles to failure was measured as a function of the disc circumferential location. Results plotted in a polar graph in Fig. 6a show a radial pattern with radial symmetry, similar to the poles found in the strain pattern induced in the cross section of the billet, during the primary forging stages

Fractography and microstructural analysis was carried out to understand the difference in fatigue behaviour. Samples were separated into “best” and “worst” performing groups in order to draw out microstructural trends. In simple crack propagation terms, the best performing set displayed a convoluted crack path where the crack steps between planes (Fig. 7a), as opposed to the worst performing set that manifested straight cracks from the surface (Fig. 7b).

The fracture surfaces analysed in the best and worst performing sets of samples do not show large differences in topography when analysed using secondary electron imaging. One of the interesting features is that faceting is not present in any of the analysed samples. This is due to the developed transformed β basketweave microstructure, where the concatenation of slip system between similar microstructural features, i.e. α laths in this case, is more complicated. This is made even more complicated due to the larger number of α variant selection and the lower diffusion levels produced by the high content of molybdenum.

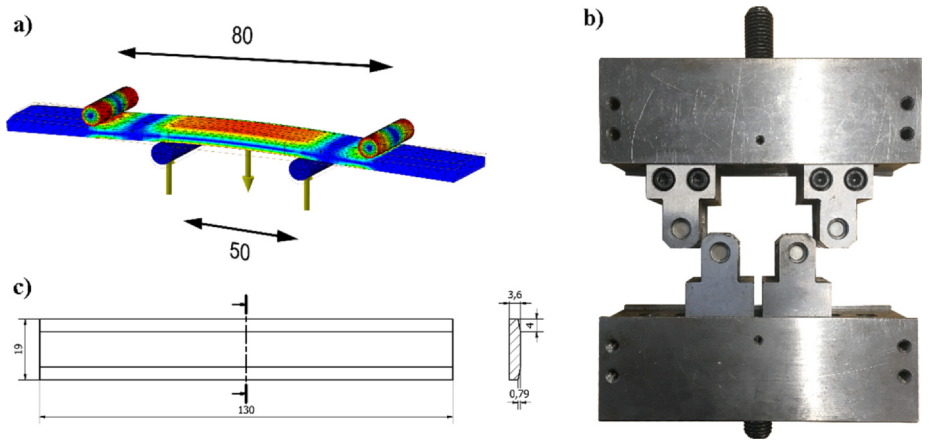

Fig. 4. (a) Schematic of the stress distribution in a 4-point bend test; (b) Photograph of the set of rollers used for the 4-point bend test and; (c) dimensions of the tested coupon (units in [mm]).

Moreover, this also means that standard fatigue striation is not present. Furthermore, in the case of all samples, cracks found in the fracture surface or in parallel planes did not seem to start at prior β grain boundaries.

Analysis performed on the cracks in Figs. 7 and 8 show the influence of microtexture on crack propagation. This feature was located in the radial face (perpendicular to the disc radius) in a perpendicular plane to the fracture surface (red face in Fig. 8a). The loading direction is parallel to the horizontal axis of the micrographs and maps shown in Figs. 8–10. This analysed crack is not the crack that led to final failure, but a side crack found in a parallel plane to the fracture surface. This micrograph and corresponding EBSD maps in Fig. 9 show the crystallographic orientation evolution for the crack propagation region. It is also worth noting that X-EDS analysis performed adjacent to the convoluted crack show no chemical segregation or abnormalities adjacent to this region. The secondary α laths transformed within the parent β grains are of a similar size and morphology in each grain. 2D Imaging of the α lath colonies can be misleading due to alignment of secondary α laths orientations in different planes. Differences in secondary α lath morphologies can be generated in regions subjected to cooling rates post forging or if there is chemical segregation [22], the latter of which was not detected in this alloy.

Fig. 9 shows detailed analysis of the crystallographic orientations at different locations along the crack. Initially, at the surface the crack is straight and perpendicular to the surface. The initial crack opening can be related to the high stresses applied to the top surface during the beginning of the test. The first deviation appears within the first prior-β grain, however within two different crystallographic orientations developed from the 12 possible variants of the Burger's relationship. In both cases (regions 1 and 2) the main crack orientation is dictated by the relative position of the applied load and the HCP c-axis, developing basal cleavage. This is a common behaviour that is repeated in regions 3, 4 and 6.

Fig. 10 shows the evolution of the Schmid factor in the texture data in favourable orientated slip in the prismatic plane. This data shows deviations or evidence of crack arresting in locations where secondary α is unfavourably orientated with respect to loading direction and the prismatic ⟨a⟩ slip $[1\ 0\ \bar{1}\ 0]\langle 1\ 1\ \bar{2}\ 0\rangle$. Such locations were observed at both grain boundaries and within the prior-β grains.

However, it is important to highlight that no other cracks were found in parallel planes to the fracture surface in any of the samples that exhibited lower fatigue performance. This could be due to the fact that the first crack that is generated in this group succeeds to failure and hence, no other cracks are created in the surface that compete with this initial crack.

Due to the circular symmetry shown in the fatigue results and the clear inheritance of the strain path induced during primary forging, an analysis on the texture of 1/4 the disc has been performed (Fig. 11).

Texture analysis of the disc shows significant variation in the multiple of uniform density (MUD) index as a function of the radial

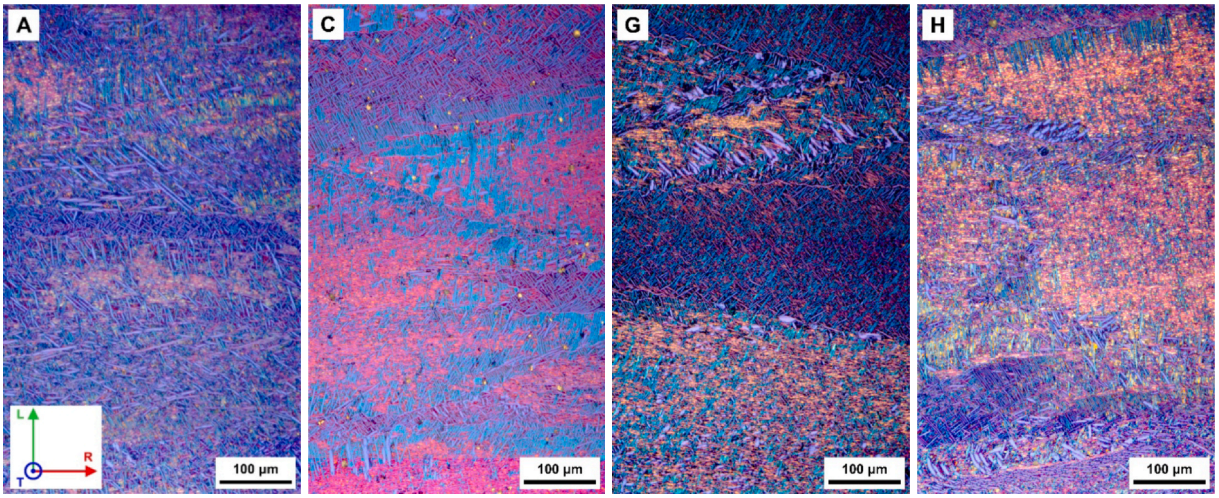

(a) 15° (b) 45° (c) 225° (d) 255°

Fig. 5. Cross polarised light micrographs of Ti-6246 at different circumferential locations of the disc after chemical etching.

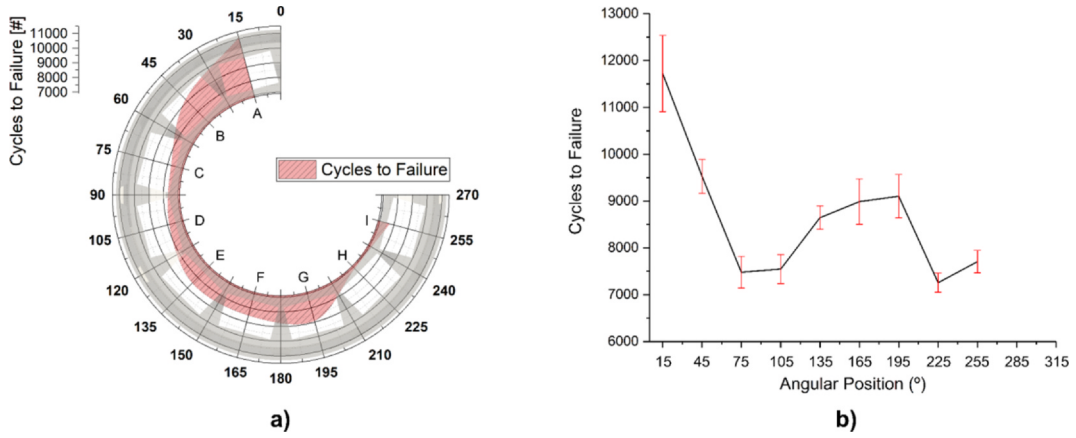

Fig. 6. Cycles to failure as a function of the radial direction for Ti-6246 rectilinear disc in the as-forged condition, shown as a; (a) Polar plot overlaid with disc section dimensions; (b) Plot of average cycles to failure and error bars (in red).

direction for the 120° segment of disc analysed. Clear effects on texture produced by upstream thermomechanical processes are observed, such as the concentric fibres and pole rotation from the secondary forging, and the broken fibres and differences in MUD scale from the strain field induced during the primary forging process. Concentric fibres shown in the (0 0 0 2) pole figures parallel to the secondary forging compression direction (L), ⟨0 0 0 2⟩//L, are characteristic of β breakdown cogging processes in titanium alloys, where the billet is forged at temperatures above the β transus temperature [23]. The MUD index variation as a function of the radial direction matches the fatigue life profile, with low textured regions presenting the longest fatigue life. It is important to show that there is preferential orientation of the c-axis with respect the tangential axis of the disc in all samples analysed.

The crack initiation mechanism was investigated for the example shown in Figs. 7–9. The EBSD map from the straight initial path is shown in Fig. 10. It shows a clear trend where the crack initiation started following a crystallographic structure which has a strong c-axis orientation parallel to the loading direction. Similar crack initiation mechanisms have been reported by Bantounas et al. [24] in high cycle fatigue analysis of Ti-6Al-4V regardless of the processing route (unidirectionally rolled, cross-rolled and forged bar), with grains orientated within 15–40° from the loading axis. Pole figures from this studied subset show a clear basal texture parallel to the X0 axis of this sample (loading direction).

In this case, the range of the angles between the crack initiation crystal structures and the loading directions is narrower than the one reported in the literature [24], in this study the range varied from 22.86° to 27.64°.

3.2. Analysis of the mechanical properties in the as-machined condition

A second Ti-6246 disc was provided by *Rolls-Royce* in order to determine the combined effect of forging and machining on fatigue performance. In this case, the component was provided in the same pre-machined stage as disc 1.

Fig. 13 shows the cycles to failure as a function of the cutting speed and the radial location from where the samples were extracted. The first key observation of this data is that regardless of cutting speed, the variation in fatigue life as a function of radial direction is still present. This data also shows that there are specific radial locations (80° and 200° respectively) in the disc that consistently under perform with respect to the average fatigue life. These locations of low cycles to failure are common in the four cutting speeds, yet are more pronounced at the lower cutting speed range between 50 and 70 m/min. Similarly, radial locations labelled as 40° and 280° are consistently higher than the average.

It is important to note that higher cutting speeds show better fatigue performance and slightly lower variability with respect to lower material removal rates and lower cutting speeds. Another interesting point from these tests is extracted from Table 3, where the average cycles to failure per radial location is calculated as a function of the cutting speed. The best average fatigue life is shown by the material machined at the fastest speed with 24,207 cycles. A direct proportional trend can be found between faster cutting speeds and longer fatigue life. However, 70 m/min falls out of this trend showing poorer performance respect the other machining speeds.

Analysis of the machined surfaces under SEM was performed to

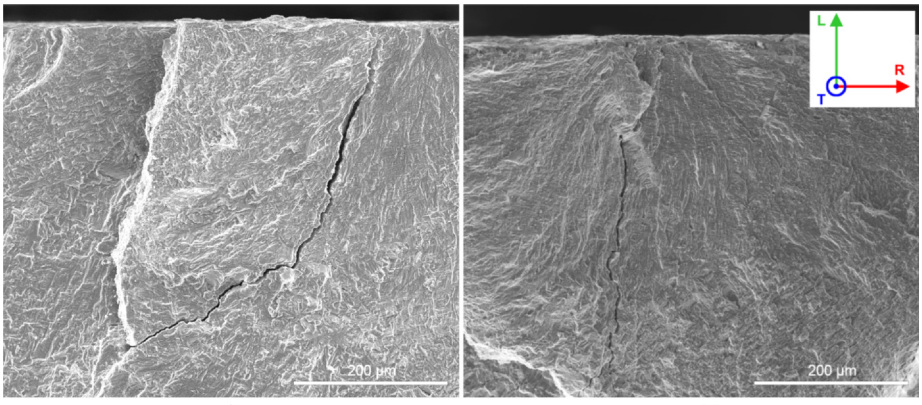

Fig. 7. Secondary electron micrographs of crack paths found in Ti-6246 fatigue coupons: (a) Shows convoluted crack path in a best performing set (G) and; (b) Shows a straight crack found in a worst performing set (H). Fractography analysis performed in the tangential plane.

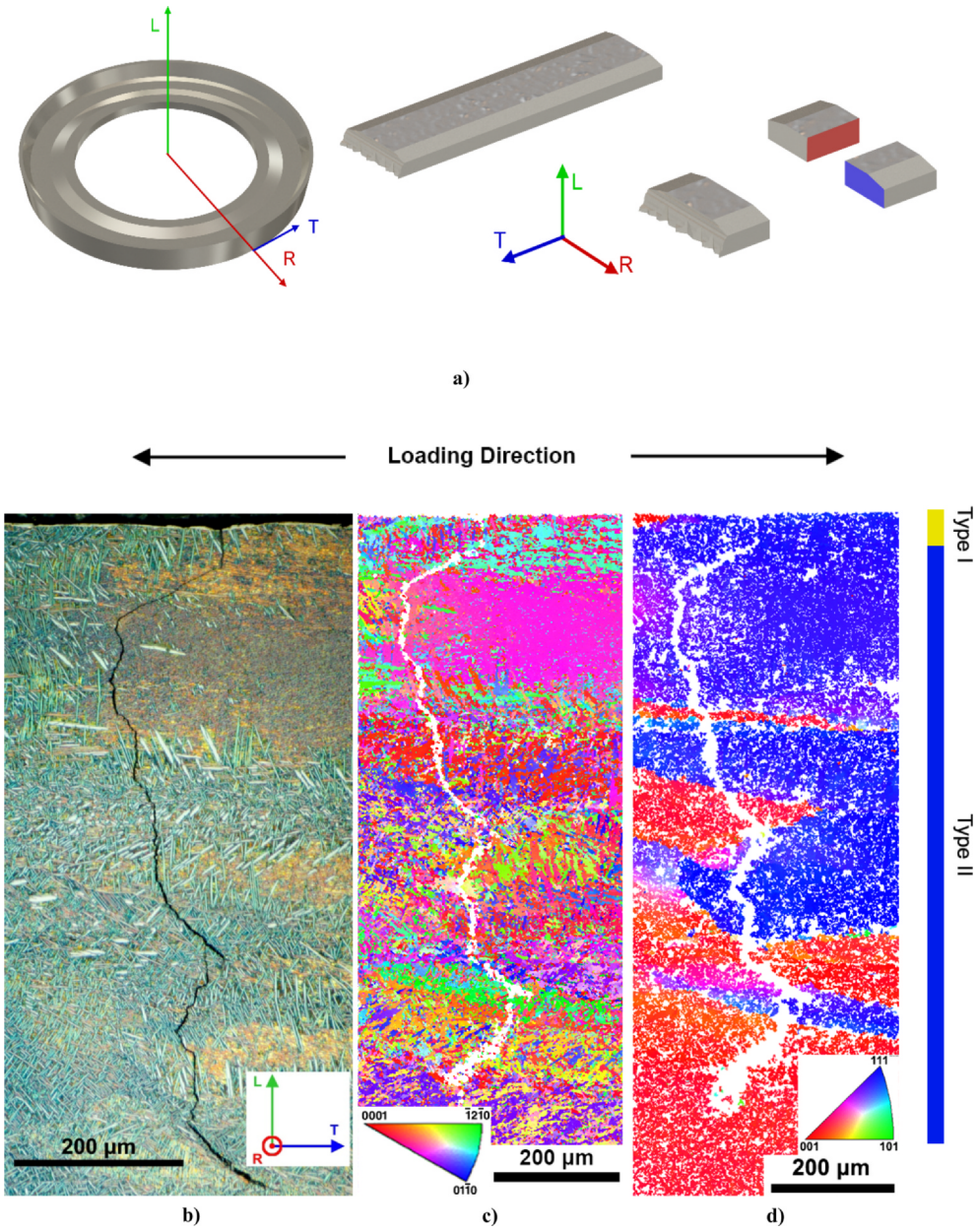

Fig. 8. Correlation between microstructure, EBSD and β reconstruction of the crack found in sample A, loading direction represented in the horizontal axis: (a) Schematic representation of analysed surface/crack location (Radial Direction) with respect to Ti-6246 disc and tested coupon: (b) Cross-polarised light micrograph of microstructure of the crack region in sample A: (c) IPF EBSD map orientated in the loading direction (T) for the crack region in sample A (C-axis represented parallel to the loading direction): (d) IPF EBSD map of the β-reconstructed regions from EBSD data for the crack region in sample A.

determine the causes of the drop in fatigue life when machined at 70 m/min. A comparison between machined surfaces machined at 50 m/min and 70 m/min is shown in Fig. 14, including tool wear at equivalent speeds. The morphology of smeared Ti-6246 material (also known as "pick up") at 50 m/min and 70 m/min are similar, however, the average size and the number of the particles at 70 m/min is greater. Such a high density of pick-up caused by built up edge at the rake of the tool that breaks away and smears under the tool flank, diffusion bonding onto the surface. Such surface protrusions reduce the fatigue performance of machined surfaces [25–30].

Tool wear has also been analysed for these two cases, with negligible wear at the cutting edge after machining at the more conservative, lower metal removal rate cutting parameters. However, substantial damage for a short finishing operation at higher machining speeds was inflicted at the cutting edge, where damage such as flank wear and built-up edge were observed.

4. Discussion

4.1. As-Forged analysis results discussion

Results analysed regarding the differences in cycles to failure (in Fig. 6) seems to correlate with the texture inherited from the non-linear strain pattern developed during the β breakdown cogging stages, specifically the lower strain axis providing 180-degree symmetry, also seen in the fatigue results. Forging appears to have a direct impact on the fatigue performance of a Ti-6246 compressor disc. This direct correlation of upstream forging dictating fatigue performance has been studied for near α titanium alloys [31–33] but never been explicitly shown before in Ti-6246 discs. It is clear from Fig. 6 that the directions A and G separated by 180°, which have the best fatigue performance, are in a similar position to the 0° and 180° position poles shown in the forging DEFORM simulation (Fig. 1a). These poles represent the lower strain

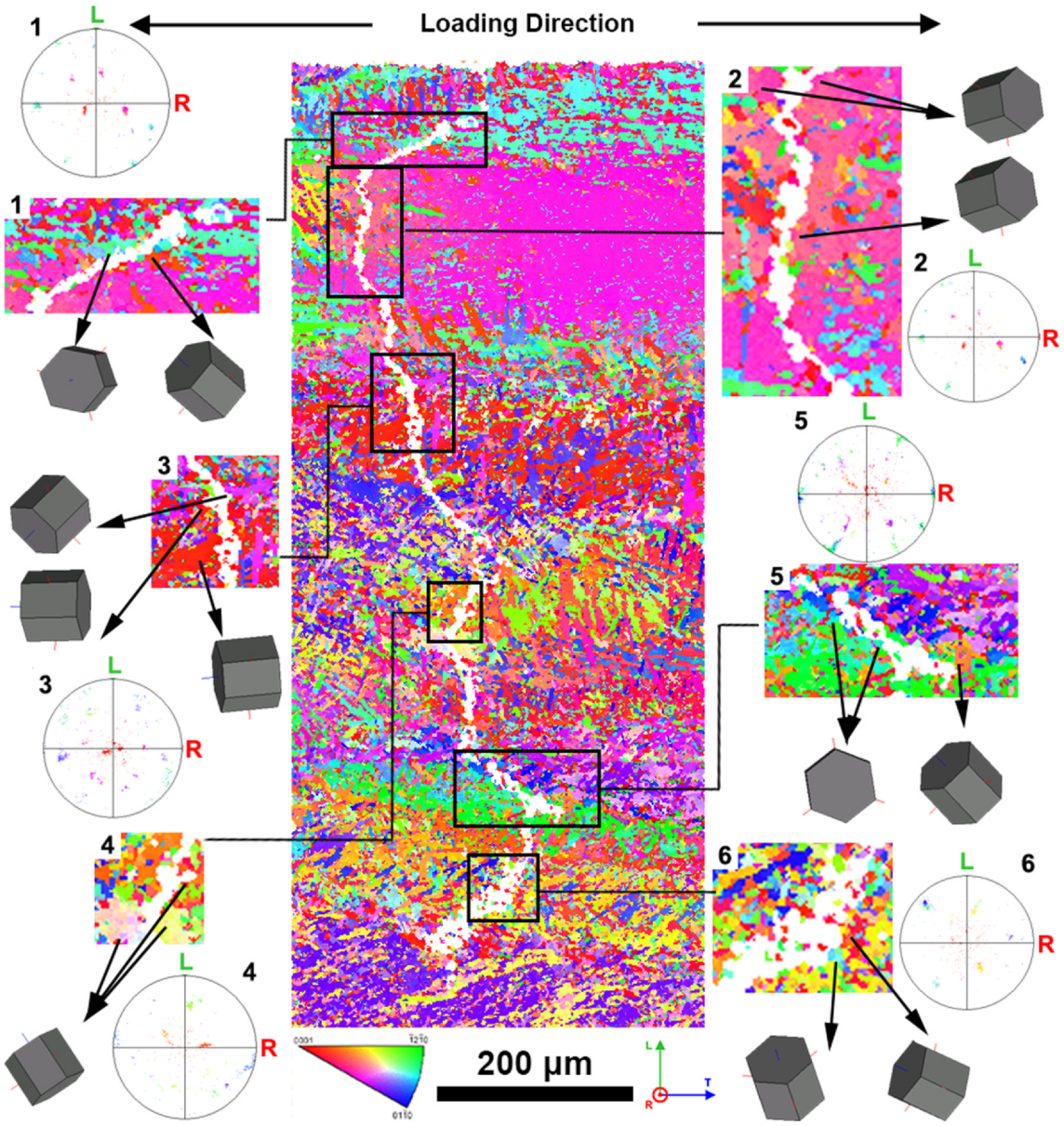

Fig. 9. EBSD map revealing the orientation of grains adjacent to the propagated crack. In the corresponding IPF colouring, the basal plane is parallel to the tangential direction of the disc (loading direction).

regions of the forged billet. This suggests that highly strained regions during the primary forging create zones of preferential anisotropic texture (higher MUD) and therefore the crack propagation time is shortened considerably due to a less convoluted crack path. It is postulated that the higher strain induced into the β crystals orientate them in a specific direction which is then transferred into the 12 different orientations available for α because of the Burger's relationship. Moreover, the preferential c-axis orientation in the tangential axis of the disc suggests that the hoop stresses applied during the secondary forging operation induces variant selection during the β to α phase transformation.

The complexity of controlling all variables involved in the forging process makes it challenging to develop a fully homogenised microstructure for the design requirement. This is because even in extremely controlled environments there is a very narrow window between breaking out the initial billet microstructure and the creation of a new strong texture as a function of the strain rate and temperature during the thermomechanical processing [30].

Fractography analysis results performed on the best and worst regions show similar fracture surface topography. However, the consistent differences in crack propagation geometry (Fig. 6a and b), imply that the crack propagation mechanisms in the best performing regions follow more convoluted paths, whereas in the worst performing regions, cracks follow the shortest least resistance path towards lower stressed regions. However, no major differences were found between the different performing samples – which exhibited similar topographical features in their fracture surfaces.

Crystallographic evolution analysis performed in a crack found in the radial direction (Figs. 8c and 9) show that the crack propagation path is dictated by the adjacent crystallographic orientation at the crack tip (Fig. 12), as well as, the driving effect of opening the crack towards the lower stress region. Studies carried out by Wilson *et al.*, showed crack propagation in HCP materials to be sensitive to local microstructure and texture [34]. However, this is a complicated system where not only the grain found at the crack tip affects the crack path; neighbouring grains also play an important role. Different crystallographic orientations in neighbouring grains lead to heterogeneous distributions and dislocation pile up and "ratcheting" of dislocations

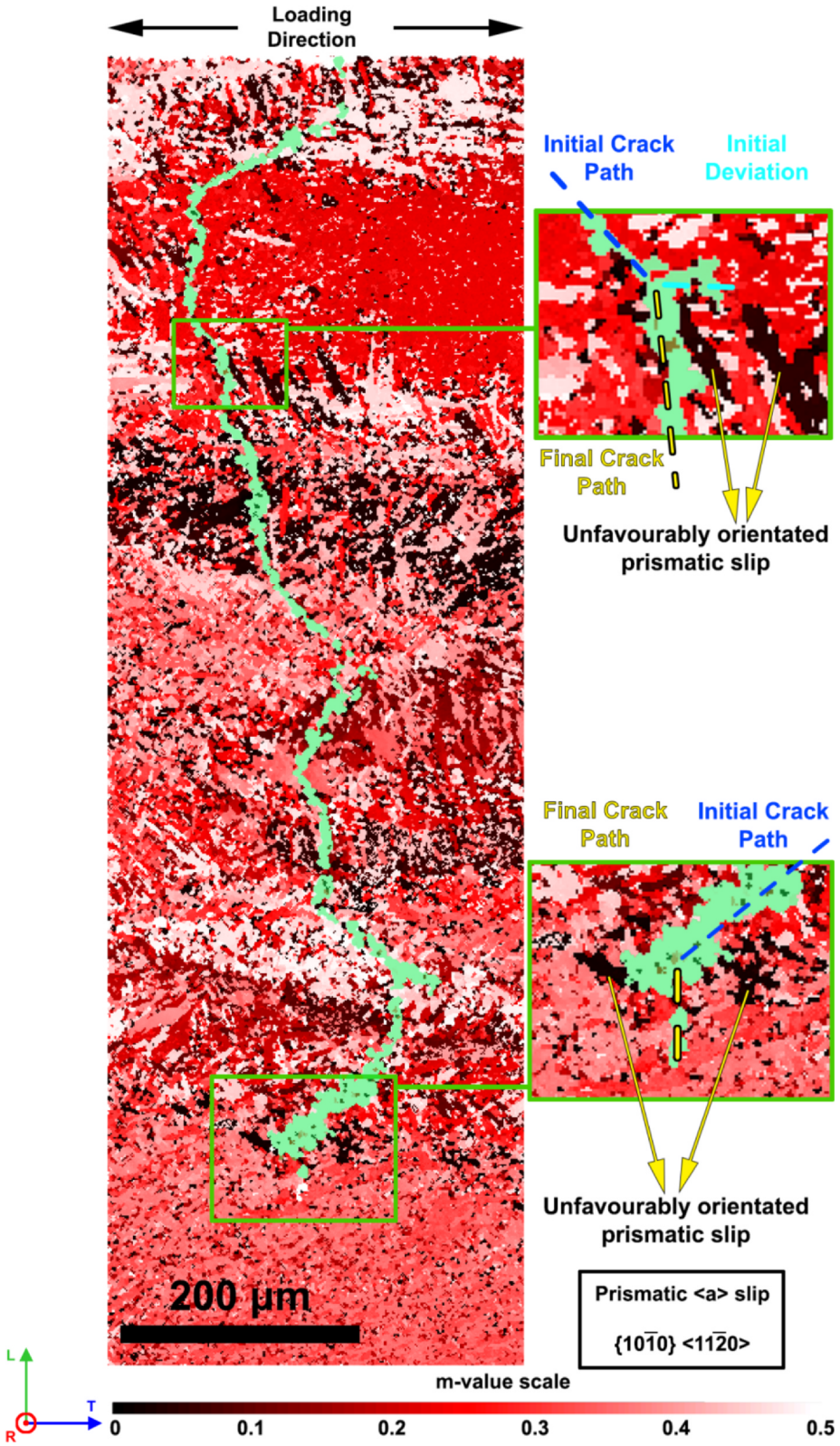

Fig. 10. EBSD Schmid factor image of the arrested crack in the Ti-6246 disc showing the crack being deflected and arrested due to the grains unfavourably oriented for prismatic slip.

from soft to hard grains [35]. This plays a critical role in dwell fatigue [36–39], but also influencing crack propagation behaviour and rates.

The role of linking texture forged heterogeneities and fatigue has been studied in near α titanium alloys such as Ti-6242 and Ti-834, as well as, the effect in fracture toughness in Ti-64 [40]. Such research provided an understanding of the effects of the subsequent strain that is induced at different locations at different stages of the production of compressor disc material. For example, Davies et al. [31] study the texture variation in the cross section of Ti-843 finding texture heterogeneities in the cross section, with a centre microstructure dominated

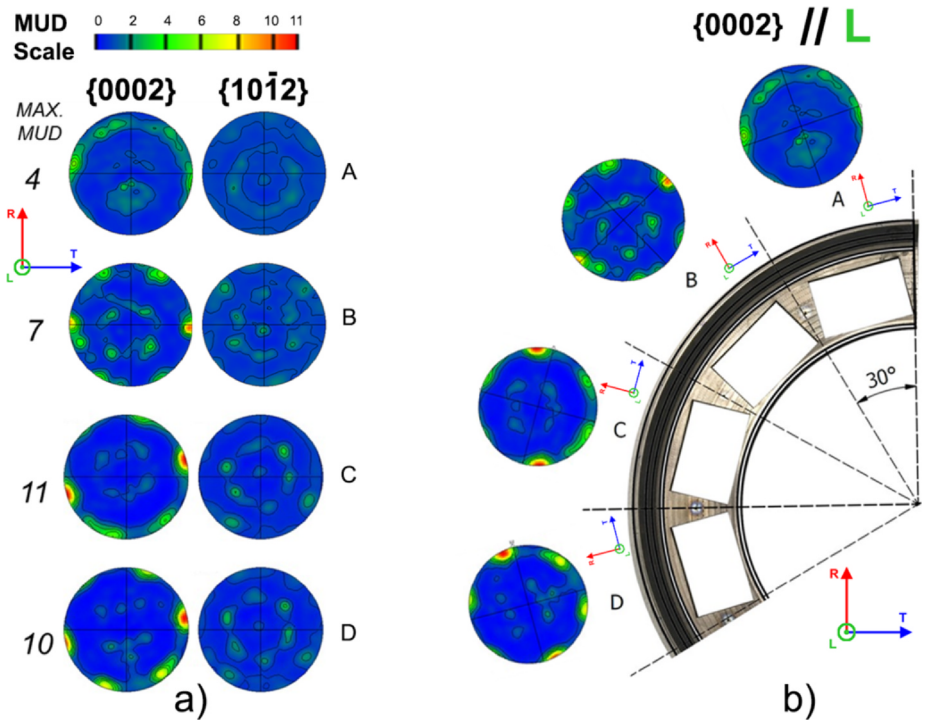

Fig. 11. (a) EBSD pole figures of the sections A-D in Ti-6246 compressor disc 1 with pole figures and (b) Representation of the pole figures under the same axes with respect to the disc.

by a {1 0 $\bar{1}$ 0} fibre-like and an outer microstructure dominated by a {0 0 0 2} component. Regarding the effect of the strain and texture development at the cross section of a compressor disc shape, Gey et al. [32] found that regions near the inner bore of the disc shape that are subjected to different strains. For example, regions where there is little change from the forging process (dead zones) macrozones are inherited from upstream processing stages.

In house β reconstruction software developed by co-author Wynne,

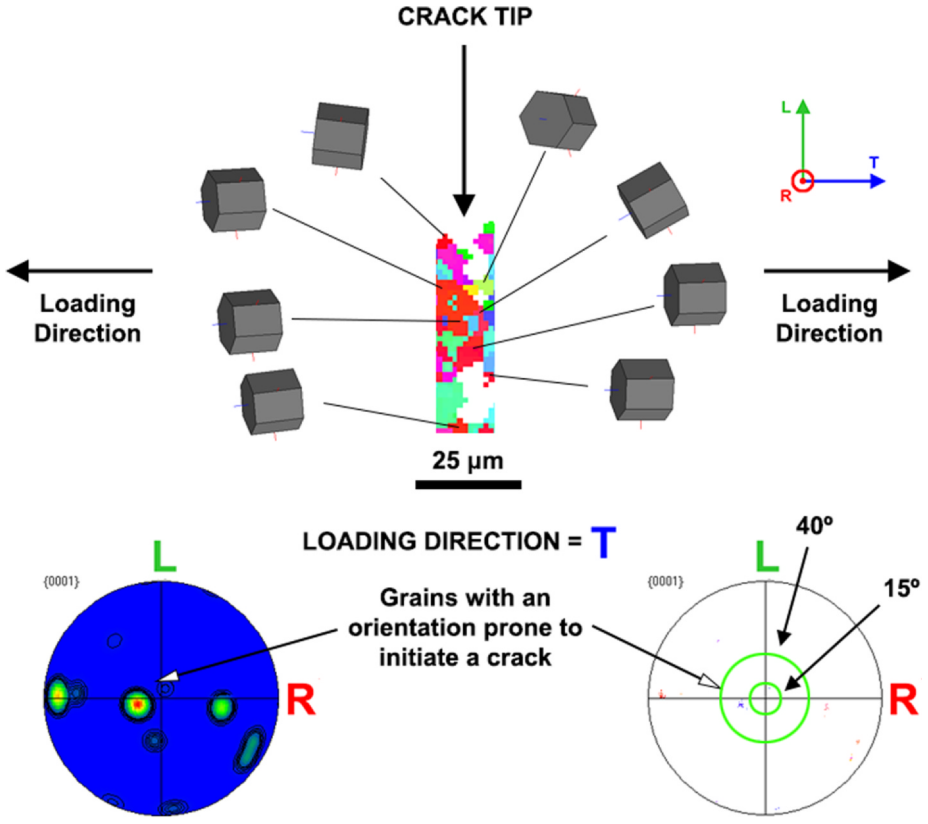

Fig. 12. Crystal orientation of the crack propagation region with main basal planes orientated parallel to the loading direction.

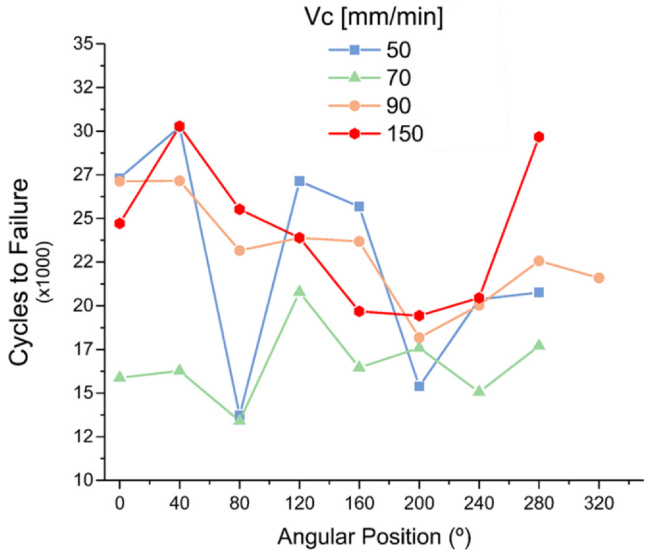

Fig. 13. Plot of cycles to failure as a function of radial direction and cutting speed of samples extracted from Ti-6246 compressor disc 2, at a range of cutting speeds.

Table 3
Average cycles of failure of all radial directions per cutting speed.

Cutting Speed [m/min]	Cycles to Failure
50	22,576
70	16,644
90	23,224
150	24,207

provided a prior β map of the surface region Fig. 8d. Such analysis clearly demonstrates that the crack deviates when crossing from one prior β grain region to another. As the prior β grain structure orientation is inherent of the primary forging stage, there is clear evidence to suggest that the crack propagation behaviour and fatigue behaviour is directly be linked to post melting cogging stage. This means that in the longer term the supply chain can develop forging strain paths that potentially enhance the fatigue performance of downstream machined compressor disc components.

Analysis of the local orientation of the HCP crystal as a function of the crack path geometry in Fig. 9 shows a clear trend, where in most of the cases, the crack propagation direction is defined by the relative orientation of the c-axis and the basal plane with respect to the crack path. This analysis is complemented with the study of the evolution of the Schmid factor with respect the loading direction and the prismatic slip systems (Fig. 10). This analysis shows that cracks are both deviated and arrested when they encounter secondary α unfavourably oriented prismatic slip planes relative to the loading direction. A similar result is reported by Bantounas et al. where the effect of crystallographic texture during fatigue loading (of dog bone samples) for Ti-6Al-4V is studied [41]. They observed that a fatigue crack arrested when it reached a structural unit size (macrozone) unfavourably oriented for prismatic $\{1\ 0\ \bar{1}\ 0\}\langle 1\ 1\ \bar{2}\ 0\rangle$. This same behaviour is clearly shown in the Ti-6246 compressor disc material, where crack arrest and crack path deviation has been found when the crack tip encounters these unfavourably oriented zones. Such crack arresting occurs due to the retardation of the crack propagation rate, as more energy is required to propagate the crack to lower stress locations, or by deviating the crack towards lower energetic paths, resulting in more convoluted path, and subsequently improving the fatigue crack propagation resistance of the component.

The difference in crack propagation is believed to have originated in the texture created during the heterogeneous strain induced during the primary forging, therefore 1/3 of the disc was analysed using EBSD.

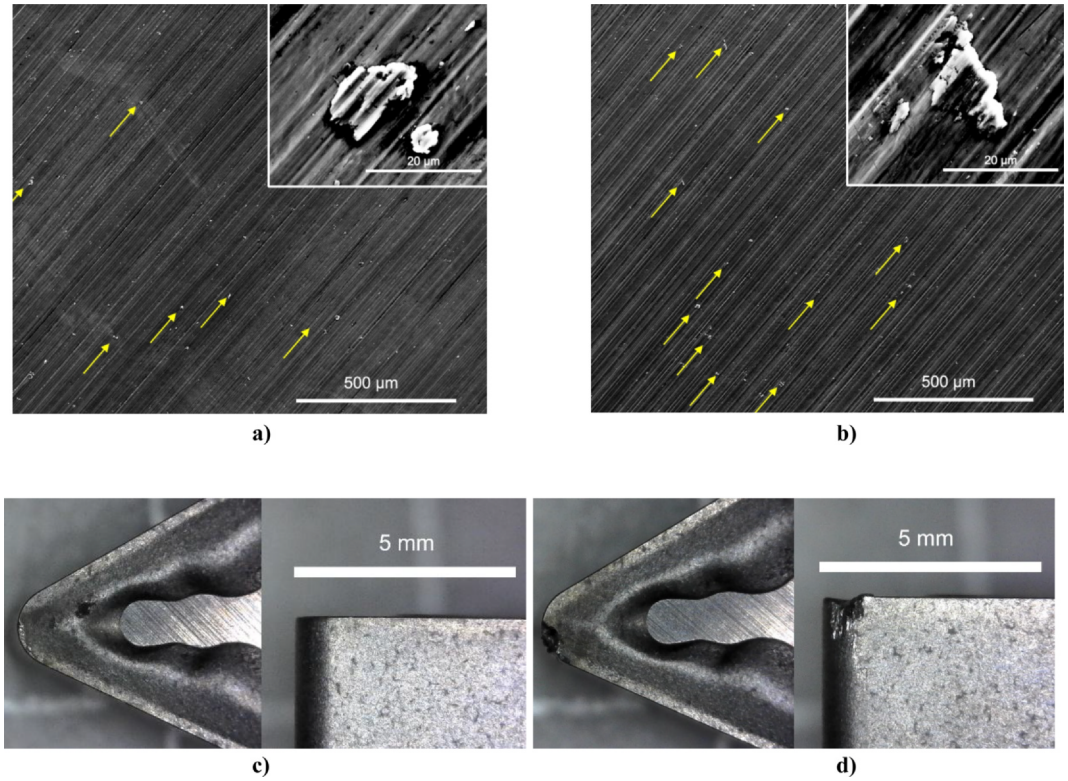

Fig. 14. Secondary electron micrographs of Ti-6246 machined surfaces with "pick up" smeared Ti-6246 deposited from the tool (highlighted with yellow arrows), at (a) 50 m/min and (b) 70 m/min. Photographs of the corresponding tool cutting tips, showing the tool abrasive wear, at (a) 50 m/min and (b) 70 m/min.

Table 4
Average cycles of failure of all radial directions per cutting speed.

Vc Cutting Speed [m/min]	Cycles to Failure
50	22,576
70	16,644
90	23,224
150	24,207

Differences in texture have been found between the analysed samples, which indicate that this is the root of the difference in mechanical properties. Moreover, the texture scale (MUD) shows significant differences, with a low MUD value of 4 representing a more random texture in the best performing locations and a higher MUD of 11 in the worst performing regions. However, it is an interesting observation that even though the texture index varies as a function of the radial direction, the c-axis of the HCP crystal is orientated in the tangential direction in all the samples analysed. This could be caused by the preferential selection of the 12 possible α developed orientations from the parent β grain. This preferential variant selection could be induced by the circumferential stress and strain during the secondary forging process, leading to the β plane (1 0 1) being preferentially orientated perpendicular to the tangential axis of the disc. The influence of the external stress applied and the α variants selected during α to β transformation has been reported by Shi et al. [42]. This would lead to a preferential creation of the c-axis for the HCP α phase in the tangential direction, as seen in Fig. 11.

The fibres that appear on the (0 0 0 2) pole figures, ⟨0 0 0 2⟩// L, can be attributed to the secondary forging based on the work of Lütjering [23]. This could be caused because the symmetry of the strain induced during this secondary forging, where the forging direction is parallel to the longitudinal axis of the component. However, based on the work of Davies [43], these fibres cannot be generated through classical dynamic recrystallisation during this forging process because of the low strain rate applied during the secondary forging and the high temperatures achieved.

Crack initiation mechanisms dependant on the crystallographic orientation have also been studied. Regions with a strong texture with a c-axis orientation between a 15° and 40° and subjected to the maximum stress are commonly the sites for crack initiation. The crack initiation mechanisms are not purely basal cleavage, an additional component of stress needs to be transferred to deformation slip in order to initiate the crack, that is believed due to the fact that no crystals with their c-axis parallel to loading direction were found at the crack initiation point. Germain et al. [33] studied the effect of the lamellar α structures developed in the parent β grain boundaries in the crack initiation mechanisms during dwell fatigue testing in Ti-6242. Although, Ti-6246 is insensitive to dwell fatigue [44], a similar correlation was found in the orientation of the HCP crystals at the crack initiation point, with the c-axis relation with the loading direction reported by Germain et al. [33] being between 18° and 22°.

No cracks were found in parallel planes to the fracture surface in the worst performing set of samples. This is attributed to the fact that the energy to propagate a crack through the structure is lower than the energy required to initiate new surface cracks.

4.2. As-machined analysis results discussion

Samples extracted from disc 2 were machined at different cutting speeds and tested under dynamic loading conditions in a 4-point bend test. The first conclusions extracted from Fig. 13 are that, even though the variability of the cycles to failure diminishes with increasing cutting speed, there remains a distinct reduction in cycles to failure at the angular positions 80° and 200°.

From the tests carried out, machining is beneficial for the fatigue life of this alloy with 2–3-fold increases in the cycles to failure in machined coupons compared to the pre-machined state. This is due to the fact that the machining process induces compressive stresses [45–47] that counteract the tensile stresses applied in the surface and subsurface layers during the fatigue bending test. However, because the machining process only affects the top 20–30 μm, it is key for the crack initiation mechanisms for two main reasons. First, the compressive stresses retard the formation of the cracks but the machining induced damage and the surface topography can counteract this, creating stress concentration points that are prone to initiate cracks. Positively, in this case, because the number of cycles to failure increased after machining, it is possible to conclude that the induced layer of compressive stresses is more dominant than the damaged microstructural layer. Moreover, no variations in the surface topography among the machined coupons at different cutting speeds are found because all the machining test have been carried out using the same feed per revolution and tool radius. In view of these results, it is also acknowledged that there will be variation in baseline fatigue data from one forging to another.

From this study, even though the machining process is beneficial for fatigue life, it does not erase the inherent effects of the forging process on texture. It is hypothesized that the severe plastic deformation from the machining process only influences the crack initiation stage and, in this case, suppresses it. The rate of crack propagation, however is dictated by the bulk microstructure, which is unaffected by the finish machining process.

Considering the average number of cycles to failure per cutting speed (Table 4), the fatigue life increases with faster cutting speeds. Interestingly from a productivity standpoint, increasing cutting speed equates to greater material removal rate and reduced machining times.

The interesting observation from Table 4 is that the results at 70 m/min deviates from the trend of increasing fatigue life. This is due to a combination of factors that promote built up edge (BUE) and crater wear on the cutting insert, determined by the observation of smeared work hardened material or “pick-up” diffusion bonded onto the machined surfaces (Fig. 14c and d). As such work hardened material from the tool BUE has diffusion bonded (or re-welded) to the surface after leaving the rake face of the tool, it has been in contact with coolant and air for a longer period of time at high temperatures. Therefore, these “pick up” protrusions increase the surface roughness and act as crack initiation points reducing the fatigue life of the component.

5. Conclusions

The as-forged material has been extensively analysed to characterise the crack initiation and propagation mechanism under dynamic loading in a low cycle fatigue experiment under high loads. The fatigue life results from the extracted samples show that there are significant heterogeneities in cycles to failure as a function of the radial location in the component. However, the radial pattern is not arbitrary and shows periodic zones with high and low fatigue performance. These radial locations are aligned with the low and high strained regions that are induced in the cross section of the billet during the primary forging stage.

The influence of the upstream forging processes and the effect of the final machining conditions used for intermediate pressure compressor disc were assessed regarding the effect in fatigue life performance, with a detailed study of the crack initiation and propagation mechanisms and their relationship with crystallographic orientations. From which we can conclude that:

1. Significant differences in fatigue life have been found in Ti-6246 disc components as a function of the radial location. This has been linked to the heterogeneous strain pattern induced during the upstream forging process, where low strained regions during primary forging showed better fatigue performance.
2. Crack propagation mechanisms activated in the locations that show

better fatigue life produce convoluted crack path geometries compared with straight cracks found in the worst performing locations.
3. A direct link between fatigue performance and texture index have been found with lower textured regions (lower MUD index) perform better under dynamic loading than regions that show higher MUD values.
4. Cracks tend to deviate and arrest when the crack tip encounters regions of secondary α unfavourably oriented for prismatic slip with respect to the loading direction, specifically in the best performing locations.
5. From the limited tests carried out, machining has been found to be beneficial for fatigue life by increments of up 2 to 3 times compared to the non-machined material, due to the compressive stresses induced during finish machining. However, it is acknowledged that there will be variation in baseline fatigue data from forging to forging.
6. Regardless of the cutting speed, texture effects from the primary forging or cogging stage influence the fatigue life as a function of the radial location.
7. Faster cutting speeds maintain and increase the fatigue life compared to more conservative machining parameters while increasing machining productivity three-fold.
8. A non-optimised cutting speed was observed at 70 m/min, which was attributed to a change in the tool/material interaction behaviour. This condition generated smeared material or pick-up on the surface as a result of BUE produced at the insert tip. Such surface features are detrimental for fatigue life, as the pick-up protrusions increases the propensity for crack initiation mechanisms at much lower cycles.

Declaration of Competing Interest

The authors declare that they have no known competing financial interests or personal relationships that could have appeared to influence the work reported in this paper.

Acknowledgements

We would like to acknowledge EPSRC grant EP/L016273 Centre for Doctoral Training in Advanced Metallic Systems for supporting this research, and Justin Davies (Sandvik) and Phil Bell, Stephen Tyas and Amber Bennett (AMRC) for advice and assistance with the trials.

References

[1] Certification Specifications for Engines CS-E. European Aviation Safety Agency [2003 last amended in December, 2018].
[2] Rugg D, Dixon M, Dunne FPE. Effective structural unit size in titanium alloys. J Strain Anal Eng 2007;42:269–79.
[3] Shamblen C, Woodfield A, Wayte P, Dilbert G. Titanium industry quality improvements. Proc 10th world conf titanium, Hamburg, Germany. 2003. p. 2737–44.
[4] Leyens C, Peters M. Titanium and titanium alloys. Wiley-VCH; 2003.
[5] Glavicic MG, Bartha BB, Jha SK, Szczepanski CJ. The origins of microtexture in duplex Ti alloys. Mater Sci Eng A 2009:325–8.
[6] Panda S, Banerjee D, Avadhani GS, Suwas S. A variant selection mechanism in the deformed and recrystallized β matrix of a metastable β-titanium alloy. Philos Mag Lett 2018:273–82.
[7] Lee E, Banerjee R, Kar S, Bhattacharyya D, Fraser HL. Selection of α variants during microstructural evolution in α/β titanium alloys. Philos Mag 2007:3615–27.
[8] Moussaoui K, Mousseigne M, Senatore J, Chieragatti R, Lamesle P. Influence of milling on the fatigue lifetime of a Ti6Al4V titanium alloy. Metals 2015:1148–62.
[9] Jawaid A, Che-Haron CH, Abdullah A. Tool wear characteristics in turning of titanium alloy Ti-6246. J Mater Process Technol 1999:329–34.
[10] Pretorius CJ, Soo SL, Aspinwall DK, Harden PM, M'Saoubi R, Mantle AL. Tool wear behaviour and workpiece surface integrity when turning Ti-6Al-2Sn-4Zr-6Mo with polycrystalline diamond tooling. CIRP Ann Manuf Technol 2015:109–12.
[11] Veiga C, Davim JP, Loureiro AJR. Review on machinability of titanium alloys: The process perspective. Rev Adv Mater Sci 2013:148–64.
[12] Arrazola PJ, Garay A, Iriarte LM, Armendia M, Marya S, Le Maitre F. Machinability of titanium alloys (Ti6Al4V and Ti-555.3). J Mater Process Technol 2009:2223–30.
[13] Armendia M, Osborne P, Garay A, Belloso J, Turner S, Arrazola P-J. Influence of heat treatment on the machinability of titanium alloys. Mater Manuf Process 2012:457–61.
[14] Thomas M, Turner S, Jackson M. Microstructural damage during high-speed milling of titanium alloys. Scr Mater 2010:250–3.
[15] Crawforth P, Wynne B, Turner S, Jackson M. The effect of turning on microstructural damage in titanium alloys. Scr Mater 2012:842–5.
[16] Thomas M, Lindley TC, Rugg D, Jackson M. The effect of shot peening on the microstructure and properties of a near-α titanium alloy following high temperature exposure. Acta Mater 2012:5040–8.
[17] Cox A, Herbert S, Villain-Chastre J-P, Turner S, Jackson M. The effect of machining and induced surface deformation on the fatigue performance of a high strength metastable β titanium alloy. Int J Fatigue 2019:26–33.
[18] Wilson AF, Venkatesh V, Pather R, Brooks JW, Fox SP. The prediction of microstructural development during TIMETAL 6-4 billet manufacturing. World conference on titanium Ti-2003. 2003. p. 321–8.
[19] Suarez Fernandez D, Wynne B, Crawforth P, Fox K, Jackson M. A novel technique to assess the effect of machining and subsurface microstructure on the fatigue performance of Ti-6Al-2Sn-4Zr-6Mo. 14th world conference on titanium (2019). 2020. (to be published by EDP Sciences, Oct 2020).
[20] Hémery S, Villechaise P. Comparison of slip system activation in Ti-6Al-2Sn-4Zr-2Mo and Ti-6Al-2Sn-4Zr-6Mo under tensile, fatigue and dwell-fatigue loadings. Mater Sci Eng A 2017;697:177–83.
[21] Channel 5 Software, Oxford Instruments. Inc.
[22] Ackerman AK, Knowles AJ, Gardner HM, Németh AAN, Bantounas I, Radecka A, Moody MP, Bagot PAJ, Reed RC, Rugg D, Dye D. The kinetics of primary alpha plate growth in titanium alloys. Met Trans A 2020:131–41. (Preprint submitted).
[23] Lütjering G. Influence of processing on microstructure and mechanical properties of (α + β) titanium alloys. Mater Sci Eng A 1998:32–45.
[24] Bantounas I, Dye D, Lindley T. The effect of grain orientation on fracture morphology during high-cycle fatigue of Ti–6Al–4V. Acta Mater 2009:3584–95.
[25] De Hosson JTM, Brebbia CA. Surface effects and contact mechanics XI: Computational methods and experiments. WIT Press; 2013.
[26] Ginting A, Nouari M. Surface integrity of dry machined titanium alloys. Int J Mach Tool Manu 2009:325–32.
[27] Zou B, Chen M, Huang C, An Q. Study on surface damages caused by turning NiCr20TiAl nickel-based alloy. J Mater Process Technol 2009:5802–9.
[28] Pawade R, Joshi S, Brahmankar P, Rahman M. An investigation of cutting forces and surface damage in high-speed turning of Inconel 718. J Mater Process Technol 2007:139–46.
[29] Souto-lebel A, Guillemot N, Lartigue C, Billardon R. Characterization and influence of defect size distribution induced by ball-end finishing milling on fatigue life. Procedia Eng 2012:343–8.
[30] Bayoumi MR, Abdellatif AK. Effect of surface finish on fatigue strength. Eng Fract Mech 1995:861–70.
[31] Davies PS, Wynne BP, Thomas MJ, Rainforth WM. IOP Conf Ser: Mater Sci Eng 2018;375:012019.
[32] Gey N, Bocher P, Uta E, Germain L, Humbert M. Texture and microtexture variations in a near-α titanium forged disk of bimodal microstructure. Acta Mater 2012;60(2012):2647–55.
[33] Germain L, Samih S, Delaleau P, Gilbert J, Gey N. Analysis of cold dwell fatigue crack initiation site in a β-forged Ti-6242 disk in relation with local texture. Metals 2020;10:951.
[34] Wilson D, Zheng Z, Dunne FPE. A microstructure-sensitive driving force for crack growth. J Mech Phys Solids 2018:147–74.
[35] Zheng Z, Balint DS, Dunne FPE. Investigation of slip transfer across HCP grain boundaries with application to cold dwell facet fatigue. Acta Mater 2017:43–53.
[36] Zheng Z, Balint DS, Dunne FPE. Dwell fatigue in two Ti alloys: An integrated crystal plasticity and discrete dislocation study. J Mech Phys Solids 2016:411–27.
[37] Stroh AN. The formation of cracks as a result of plastic flow. Proc R Soc Lond A: Math 1954:404–14.
[38] Dunne FPE, Rugg D. On the mechanisms of fatigue facet nucleation in titanium alloys. Fatigue Fract Eng M 2008:949–58.
[39] Dunne FPE, Rugg D, Walker A. Lengthscale-dependent, elastically anisotropic, physically-based hcp crystal plasticity: Application to cold-dwell fatigue in Ti alloys. Int J Plast 2007:1061–83.
[40] Buirette C, Huez J, Gey N, Vassel A, Andrieu E. Study of crack propagation mechanisms during Charpy impact toughness tests on both equiaxed and lamellar microstructures of Ti–6Al–4V titanium alloy. Mater Sci Eng A 2014;618:546–57.
[41] Bantounas I, Lindley TC, Rugg D, Dye D. Effect of microtexture on fatigue cracking in Ti–6Al–4V. Acta Mater 2007:5655–65.
[42] Shi R, Wang Y. Variant selection during α precipitation in Ti–6Al–4V under the influence of local stress – A simulation study. Acta Mater 2013;61(16):6006–24.
[43] Davies P. An investigation of microstructure and texture evolution in the near-alpha titanium alloy timetal 834 PhD thesis UK: The University of Sheffield; 2009.
[44] Qiu J, Ma Y, Lei J, Liu Y, Huang A, Rugg D, et al. A comparative study on dwell fatigue of Ti–6Al–2Sn–4Zr–xMo (x = 2 to 6) alloys on a microstructure-normalized basis. Met Mater Trans A 2014;45:6075–87.
[45] Ulutan D, Ozel T. Machining induced surface integrity in titanium and nickel alloys: A review. Int J Mach 2011:250–80.
[46] Machado AR, Wallbank J. Machining of titanium and its alloys-a review. Proc Inst Mech Eng B J Eng Manuf 1990:53–60.
[47] Abboud E, Attia H, Shi B, Damir A, Thomson V, Mebrahtu Y. Residual stresses and surface integrity of Ti-alloys during finish turning –guidelines for compressive residual stresses. Procedia CIRP 2016:55–8.